International Journal of Refractory Metals and Hard Materials 126 (2025) 106950

Contents lists available at ScienceDirect

International Journal of Refractory Metals and Hard Materials

journal homepage: www.elsevier.com/locate/IJRMHM

Void formation driven by plastic strain partitioning during creep deformation of WC-Co

L. Weller [a], R. M'saoubi [b,c], F. Giuliani [a], S. Humphry-Baker [a,*], K. Marquardt [a,d,*]

[a] Department of Materials, Imperial College London, Prince Consort Road, London, SW7 2BP, UK
[b] R&D Materials and Technology Development, Seco Tools AB, Björnbacksvägen 2, 737 82 Fagersta, Sweden
[c] Division of Production and Materials Engineering, Lund University, Ole Römers väg 1, 22100 Lund, Sweden
[d] Department of Materials, University of Oxford, Parks Road, Oxford OX1 3PH, UK

ARTICLE INFO

Keywords:
EBSD
Tungsten carbide
Hardmetals
High temperature creep

ABSTRACT

Creep deformation of WC-Co composites at high temperature and stress is accommodated by either bulk WC creep or by Co-infiltrated grain boundary sliding. It has been proposed that certain grain boundaries are more susceptible than others to such sliding, and depending on the applied stress, the overall deformation rate can be limited by either mechanism. Here, we have used Electron Back-Scatter Diffraction to study the strain partitioning in each phase, the evolution in phase boundary and grain boundary misorientation, and void formation. Several WC-Co samples (Co contents ranging 7–13 % and grain sizes 0.5–1 μm) were deformed by unconstrained compression at 1000 °C under constant load in the range 0.5–1 GPa. The localised deformation state – as characterised by increases in pixel misorientation and inverse pole figure dispersion – increased significantly between 0.5 and 0.75 GPa for both phases, which may be associated with the onset of grain boundary sliding. The onset of the formation of creep voids occurred when the stress level was 0.75 GPa or more. Deformation was correlated with an increase in 60° Co_{FCC} /Co_{FCC} boundaries, and in 56° WC/Co_{FCC} boundaries. Boundaries with the latter misorientation angle may preferentially enable the Co infiltration process.

1. Introduction

Tungsten carbide-cobalt hardmetals remain the most widely used hard ceramic-metal composites. The presence of the Co binder provides fracture toughness and thermal shock resistance, while WC contributes the necessary strength and hardness. This flexibility provides unparalleled performance across technical industries such as oil and gas exploration, mining and metal cutting [1]. For many of these applications, the properties must also be retained at high temperature. In the metal cutting industry, increasing the cutting speed can improve production efficiency. This is at the cost of greater mechanical and thermal loads, which induces more plastic deformation, leading to gradual shape change of the tool which renders it unusable [2]. Thus, minimising deformation of the cutting tool edge could lead to extended tool lifetimes. This may be achieved if the complex interaction of the active deformation mechanisms is better understood.

The mechanical behaviour of WC-Co can be classified in three temperature regimes [3]: (1) below 500 °C, the material behaves elastic-brittle manner; (2) between 500 and ~ 800 °C, some plastic deformation is enabled in the metal binder, but extensive plasticity is prohibited by the immobile WC skeleton; and (3) above 800–900 °C deformation of the WC skeleton becomes enabled by infiltration of grain boundaries (GBs) by Co [3], enabling extensive deformation. Most work has focussed on characterising the high temperature regime, where the rate limiting step at a given temperature depends on the strain rate [4]. At low strain rates, WC-WC GBs are inactive, the corresponding stress exponent is high (n = 4–6), and deformation is limited by power law creep of the WC skeleton [4]. At intermediate strain rates, the deformation is found to localize in the weaker Co binder phase; Co infiltrates the WC/WC GBs, leading to GB sliding [5]. There is a corresponding drop in the stress exponent to about $n = 1$. Finally, at higher strain rates, the stress exponent increases again to $n = 4$–6, which has been attributed to a return to power law creep in the WC phase being the rate limiting process, once sliding of all the available GBs has been activated [4]. Thus, the transition between regimes and the related deformation resistance is largely controlled by WC/WC boundary infiltration.

Attempts to better understand boundary infiltration during creep are so far limited. DFT simulations highlight that higher energy GBs are

* Corresponding authors.
E-mail address: shumphry@ic.ac.uk (S. Humphry-Baker).

https://doi.org/10.1016/j.ijrmhm.2024.106950
Received 13 September 2024; Received in revised form 1 November 2024; Accepted 1 November 2024
Available online 2 November 2024

accompanied by a reduced order at the GB [6], suggesting that they may be less stable and hence susceptible to preferential binder infiltration. This is supported by Electron Back-Scatter Diffraction (EBSD) experiments of binder infiltration during sintering [7]. Generally, a strong bias in the misorientation distribution amongst WC/WC GBs is observed, resulting in a high frequency of low-energy 90° misorientation angles, also known as Σ2 GBs. Other low energy GBs include twins as well as coincidence site lattice GBs. The majority of Σ2 GBs are already present in powder form [8]. Certain low energy GBs such as the Σ2 coincidence site lattice boundaries [9], are thought to be mostly resistant to Co infiltration, based on calculation [10] and experimental evidence [11]. For instance, pre- and post-mortem examination of cemented carbide cutting inserts showed that about 10–20 % of carbide-carbide boundaries separate and are infiltrated by the binder during creep [2]. It has previously been suggested that Co-binder forms continuous layers infiltrating between WC-WC grains, yet Mingard et al. observed that the Co-binder commonly forms multiple discrete precipitates at boundaries and suspect that precipitation is more common on random boundary orientations, which favour infiltration. Whereas grain boundaries between prism/prism, prism/basal or basal/basal planes show no infiltration [5].

In addition, special low energy interfaces can accommodate strain as dislocations may cross the GB more easily compared to more random GBs where dislocations accumulate and concentrate stress [10]. Thus, in general it can be hypothesised that low energy interfaces prevent infiltration, grain boundary sliding (GBS), and creep deformation of the system as a whole. Understanding their relative fractions and their evolution during WC deformation may allow making better design choices.

The situation is further complicated by other factors that can affect creep behaviour, including the WC grain size [12], the crystal structure of the Co matrix [13], its volume fraction [9,12] and alloying additions [12]. The Co structure in particular is controlled by the content of dissolved C and W. Experiments on dilute Co-W-C alloys simulating the composition of the binder show that at lower dissolution amount the face centred cubic (fcc) crystal structure of Co is stable, while at higher W and C contents, Co takes both the cubic fcc and the hexagonal closed packed crystal structure (hcp) [14]. The relative amount of fcc phase has been shown to decrease during tensile plastic deformation [14].

It is also important to consider the tertiary creep stage, which is characterised by formation of pores and voids, which lead to stress concentrations and attendant failure [15,16]. These creep voids occur in WC-Co when the binder is no longer able to infiltrate the space between separating grains efficiently enough [17,18]. Östberg and Andren suggest that the process of Co boundary infiltration, driven by stress-assisted dissolution, may itself aid void formation given the directional diffusion of cobalt vacancies away from the interface. However, it is not clear whether the magnitude of vacancy migration can account for number and size of observed voids [5]. Nevertheless, the nucleation of voids due to high hydrostatic stress states has also been observed in finite element simulations [19].

Our study attempts to correlate deformation induced changes in grain boundary misorientation, pore formation, and localised deformation in each phase via EBSD. We deform the samples at 500–1000 GPa and 1000 °C for a test matrix of four samples: coarse/fine and high/low Co contents. The results are organised in four sub-sections: (1) the macroscopic stress-strain behaviour; (2) localised deformation characteristics of the grain interior; (3) the evolution of grain boundary misorientation; and (4) pore morphology. Below a strain of 7–10 %, the deformation is generally accommodated by deformation in the Co phase, while above that creep in the WC phase occurs and is accompanied by significant void formation.

2. Methodology

The samples were (4x4x8 mm) cuboids that were extracted from WC-Co cutting inserts of the following ISO type geometry SNUN120400. The inserts were manufactured by Seco by milling and mixing WC and Co powders, pressing into a green shape and finally sintering in vacuum at ~1500 °C. Table 1 details the set of samples analysed.

Samples were deformed in a vacuum furnace (Materials Research Furnaces) within a 20 kN load cell. The furnace had molybdenum heat shields, tungsten heating elements and graphite push rods. The samples were heated to 1000 °C and once the temperature stabilised, loaded at 25 N/s up to a set-point load that corresponded to an initial stress state of 0.5, 0.75, or 1 GPa. Samples were held under this load for 12 min (except the 13C samples tested at 1 and 0.75 GPa, where the time was reduced to 1 and 8 min respectively to prevent excessive deformation). This was followed by unloading at 25 N/s and furnace cooling.

Scanning Electron Microscopy (SEM) was performed in a Sigma VP microscope from Zeiss. The Electron Back-Scatter Diffraction (EBSD) analysis was conducted using an accelerating voltage of 20 kV, a 120 μm aperture, 10,000× magnification, a 0.05 μm step size, and a 16 mm working distance.

To investigate the creep induced changes in grain structure, grain boundary misorientation and the formation and distribution of voids, data analysis was conducted using Fiji (ImageJ) and MatLab's MTex toolbox [20]. Using Fiji's analyse particles tool, the average area and area fractions of voids in all samples were determined via an average of measurements taken at magnifications of 2 K, 5 K, and 10 K. To determine the orientation relationship of the microvoids, voids consisting of a minimum of 12 pixels were best-fit with ellipses.

3. Results and discussion

3.1. Deformation behaviour

Fig. 1 shows the deformation curves for all samples tested. The nominal engineering strain is plotted, which is equivalent to the cross-head displacement divided by the starting specimen height. The materials underwent a preliminary period of elastic deformation of 40–80 s to a nominal engineering strain of 5–10 % depending on the applied load (NB – this nominal engineering strain is not equivalent to the sample engineering strain as it includes elastic strain of the instrument, which is corrected for in Table 2).

Once the maximum load is reached the slope of the deformation curves reduces and the samples continue to deform plastically a further 3–21 % depending on the sample and applied load. The additional plastic strain can be attributed solely to creep deformation as there is no further deformation of the instrument due to the constant applied load. The residual engineering plastic strains during this period of creep deformation are noted in Table 2. We note that the true strain will be higher due to an increase in cross-sectional area of the specimens, as well as some creep deformation occurring during the specimen loading phase, which is not accounted for in our calculations.

3.2. Grain volume

Fig. 2 shows the grain size distributions of the WC particles for the as-

Table 1
Summary of the sample characteristics and mechanical testing conditions of the four samples tested in this study. The sample ID indicates both the Co content and WC grain size classification. The nominal stresses at which each sample was tested are indicated along with the duration of the test in minutes.

Co content (vol%)	WC grain size classification	Sample ID	Grain refiner additions	0.5 GPa stress	0.75 GPa stress	1 GPa stress
7	fine	7F	Cr	12 m	/	12 m
8	coarse	8C	Ta/Nb	12 m	/	/
13	fine	13F	Cr	/	/	/
13	coarse	13C	Cr	12 m	8 m	1 m

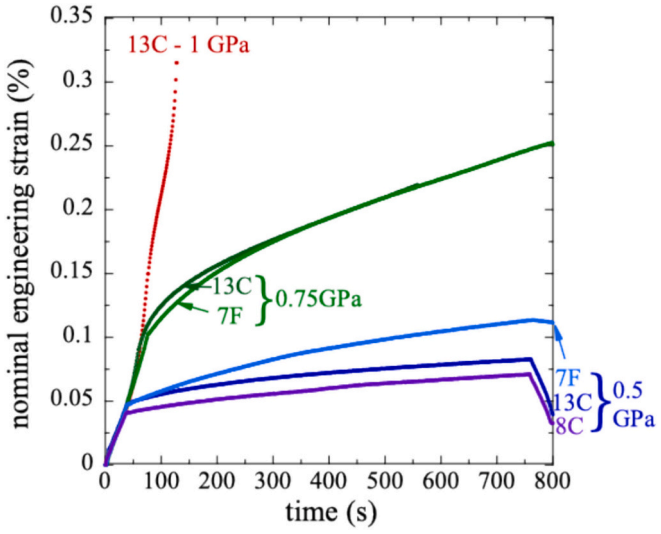

Fig. 1. Plot of nominal engineering strain vs. time for all samples characterised.

Table 2
Nominal elastic strain, total strain, and residual engineering plastic strain for each test.

Sample	8C-0.5GPa	7F-0.5GPa	7F-1GPa	13C-0.5GPa	13C-0.75GPa	13C-1GPa
Elastic	0.041	0.047	0.103	0.048	0.092	0.103
Total	0.071	0.113	0.251	0.083	0.219	0.315
Plastic	0.03	0.066	0.148	0.035	0.127	0.212

sintered and crept samples. The fine powders yielded distributions with a lower modal grain diameter of 0.5 μm, and showed no significant effect of binder volume fraction. However, for the coarse WC particles with a modal diameter of about 1 μm the size distribution varied with binder content. The 8 % Co samples showed a peak at 0.8 μm, while for the 13 % Co samples the peak was at 1.05 μm and the distribution was slightly broader. For both the fine and coarse materials, the size distribution did not change during creep deformation.

We used MTex to determine a pixel average misorientation with respect to all of its neighbour pixels - the kernel average misorientation (KAM). Before calculating the KAM we denoised the EBSD data using the half-quadratic minimization on manifolds as described in [21]. This filter removes spatially independent noise. We calculated the KAM to the 1st order neighbour pixel and used a threshold angle, $\delta = 2.5°$. This analysis highlights distortions in the crystal lattice as being regions of particularly high dislocation density. The KAM maps are shown in Figs. 3 and 4.

Fig. 3 shows a general increase in KAM within the WC grains as the stress increases. At low stress levels of 0.5 GPa the overall KAM is identical to the undeformed state, both being on the order 0.1–0.13°, depending on the sample (average KAM indicated in sub-figure insets at top-left). The existing misorientation is visible as fine bands of localised plastic deformation that tend to coincide with contact points between adjacent WC grains. The lack of any change in average KAM at low stress is confirmed by the histograms in Supplementary Fig. 1, which show almost perfect overlap of the misorientation distribution data for 0 and 0.5 GPa. (Note: Angular resolution of EBSD is determined by the analysis method. 'Traditional EBSD' utilises peak detection within the Hough transform and a look up table of interplanar angles to determine the absolute crystal orientation. Using this method, the absolute crystal orientation can be determined to an accuracy of 2° [22] and relative misorientation can be determined to a sensitivity of ~0.5° [23]). This suggests that the majority of KAM in the 0.5 GPa samples results from sample processing. The presence of these local deformation features may be explained by the considerable residual compressive stresses expected in WC grains after cooling from the sintering temperature (e.g. ~500 MPa at 10 vol% Co [24]).

Fig. 4 shows the KAM data for the Co binder. Unlike the WC phase, there is a measureable increase in average KAM for all samples at the lowest stress level of 0.5 GPa. This is supported by the misorientation distribution data in Supplementary Fig. 1, which clearly shows a discernible shift in the misorientation distribution between 0 and 0.5 GPa for the fcc Co phase, but no discernible shift for the WC phase.

As the stress increases to 0.75 and 1 GPa, Fig. 4 shows increasing KAM, with thicker and more frequent deformation bands. The magnified regions shown for the 0 and 0.5 GPa deformed samples exhibit about 1 fine band per grain, ~100 nm in thickness, whereas at 1 GPa deformation the several grains exhibit 3–4 bands that are 200–300 nm or more in thickness. This is supported by the continued increase in average KAM. For example, in the 13C sample, the mean KAM increased from 0.14 in the reference state to 0.23° for the 0.75 GPa sample, and to 0.3° for the 1 GPa sample. The misorientation distribution data in Supplementary Fig. 1 also shows a marked and progressive change in the misorientation distribution. The final increase in mean KAM was ~60 and 110 % compared to the reference state, for the 0.75 and 1 GPa samples respectively. This is comparable to the increase in mean KAM for the WC

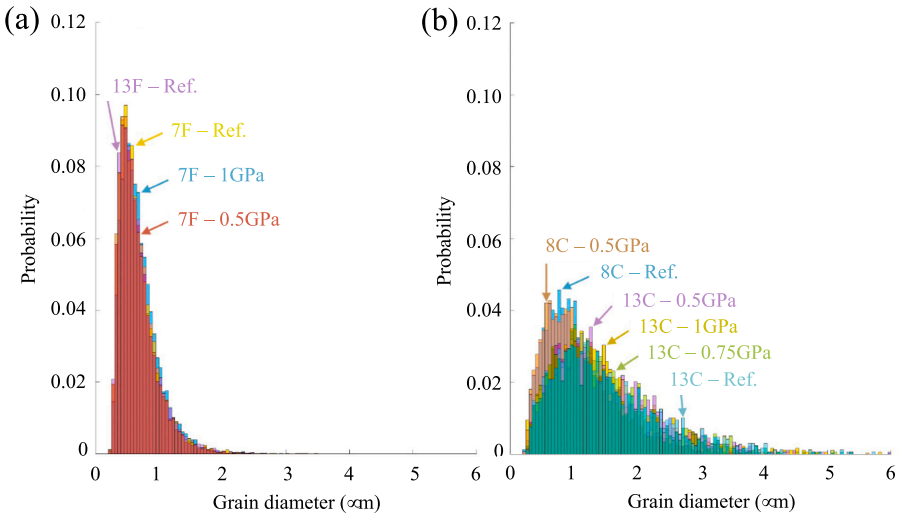

Fig. 2. Grain/particle size distributions of samples with (a) fine and (b) coarse WC particles. There is little change due to creep deformation.

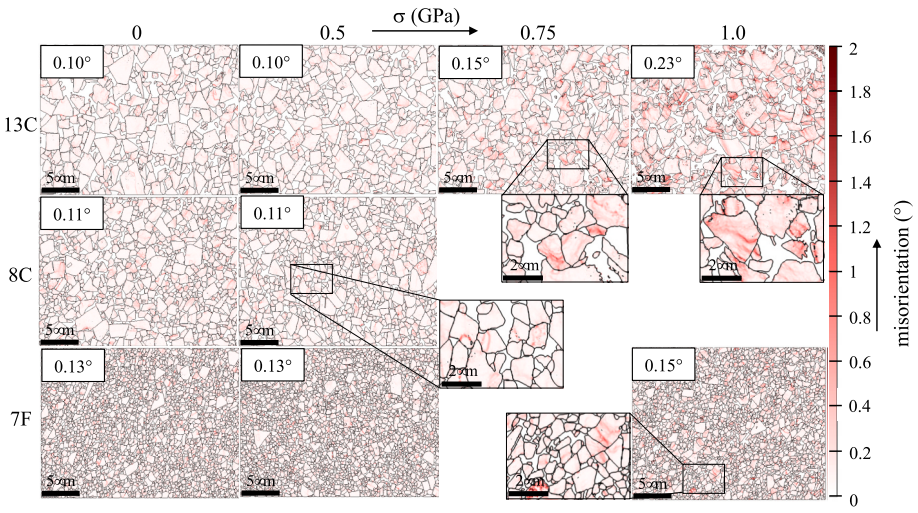

Fig. 3. One representative KAM map in the WC grains for each of the deformed samples displayed for the available levels of stress and respective grain sizes. The average KAM is indicated in the top-left of each sub-figure. Magnified regions of highly deformed grains show strain bands.

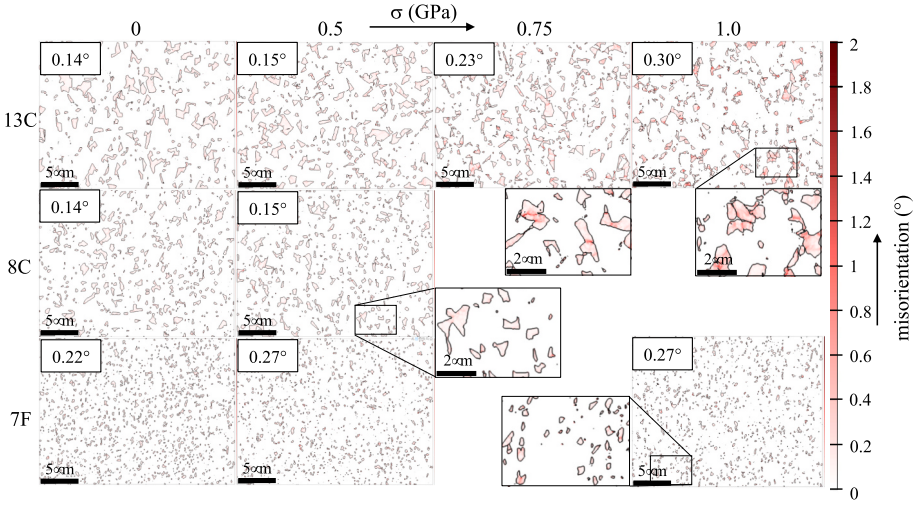

Fig. 4. KAM map within the Co grains for all deformed samples at all available levels of stress. The average KAM for the dominant fcc phase is indicated in the top-left of each sub-figure. Magnified regions of highly deformed grains show strain bands.

phase, which was ~50 and 130 %. The similar levels of increase is perhaps surprising given the lower flow stress in the Co, but may be explained by its higher rates of defect recovery.

To depict the long-range deformation of the binder grains, inverse pole figure (IPF) maps were constructed Figs. 5 & 6. Note: in these figures we have only shown the orientation plots for the reference states, as the plots for the deformed states appeared qualitatively similar. For the WC grains (Fig. 5), the orientation plot in the reference state shows several hundred randomly oriented grains. The corresponding IPF map shows each corresponding grain as a closely packed group of dots (pixels), indicating each grain has a narrow range of orientations. For the finer grained sample (7F), the grouping of the dots is less obvious, due to the larger number of grains, and the fewer pixels in each grain. The 0.5 GPa IPF maps appear qualitatively similar, which agrees with the lack of change in localised misorientation of the WC grains for these samples shown in Fig. 3. By comparison, the 0.75 and 1 GPa samples show a progressive dispersion (un-grouping) of the orientations belonging to each WC grain. This indicates significant longer-range deformation has accumulated in those grains in agreement with the overall macroscopic sample strain, with the 0.5, 0.75 and 1 GPa samples accommodating strains of ~3.5, 12.7 and 21.2 %, respectively (Table 2).

The orientation plots for the Co grains in Fig. 6 show markedly fewer grains. For example, only two grains are shown for the 13C sample, 4–5 grains for 8C, and 8–10 grains for 7F. This trend is representative across four different areas of interest for each sample. The increase in number of Co grains with decreasing grain size and Co content is accompanied by an increase in the dispersion of the orientation in each grain, with the highest dispersion being seen in 7F. The high dispersion in the 7F sample can be associated to the higher anticipated residual stress state in the Co phase that results from a combination of fine microstructure and low binder content. This observation supports previous X-ray diffraction measurements of residual stress in the binder phase, which find that the stress is significantly higher in Co compared to WC and can exceed 3 GPa in fine grained materials with low binder content [24].

Considering the effect of applied stress on the Co IPF maps: there is a more pronounced spreading of the orientations than was seen for the WC maps. Furthermore, there is spreading even at 0.5 GPa, which was not observed in the WC grains. This observation agrees with the KAM maps in Figs. 3 & 4 in their conclusion that deformation is accommodated predominantly in the Co phase at 0.5 GPa. At 0.75 and 1 GPa, the poles in the IPF maps diverge even further, such that individual grains, or clusters, are no longer distinguishable.

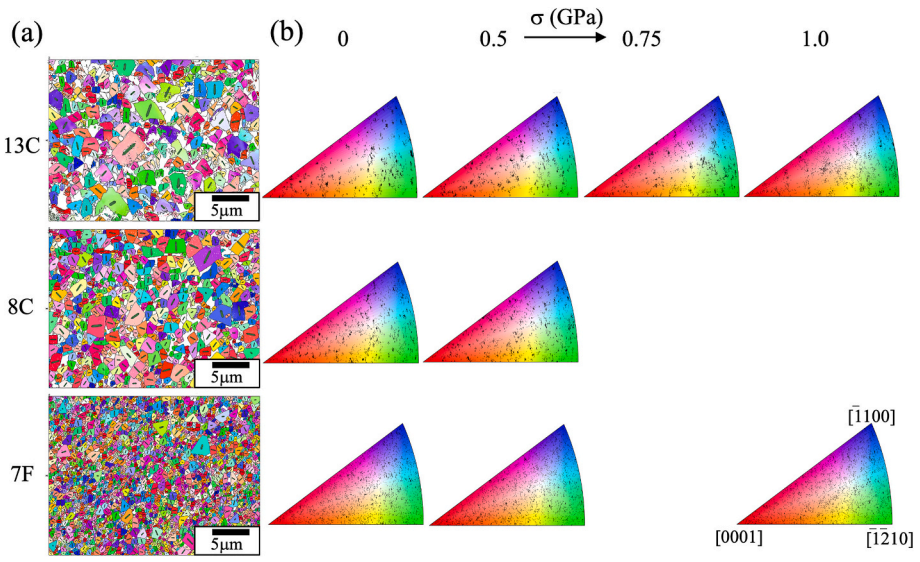

Fig. 5. (a) orientation plot for WC grains in reference state (0 GPa) and (b) Inverse Pole Figure (IPF) for WC grains in all samples, highlighting the deformation with respect to a global axis. All IPFs are indexed identically, but only the index for the 7F sample at 1 GPa is shown for figure clarity.

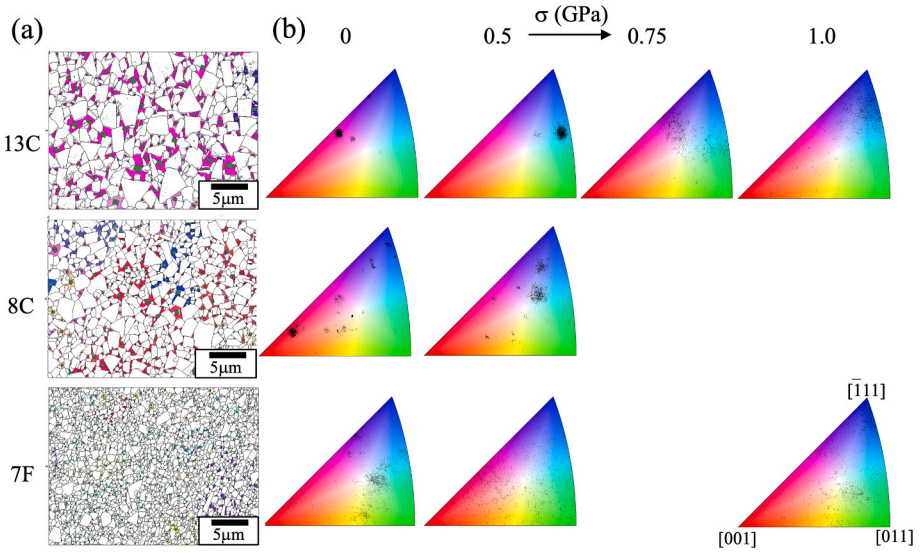

Fig. 6. (a) orientation plot for Co grains in the reference state (0 GPa) and (b) Inverse Pole Figure (IPF) for Co grains in all deformed samples (0–1.0 GPa), highlighting the deformation of the binder grains with respect to a global axis. Again, only the index for the 7F sample at 1 GPa is shown for figure clarity.

The onset of significant localised deformation in the WC phase between 0.5 and 0.75 GPa, as shown by Fig. 5, and by the significant deformation band formation (Fig. 3) – may be related to a change in the dominant deformation mechanism. It is interesting to note that the threshold stress for deformation in WC is similar to the yield strength of ~700 MPa that was found for WC-10.5Co (1 μm average grain size), when loaded monotonically in compression at 5×10^{-3} s^{-1} and 900 °C [25]. In literature creep experiments, a drop in the activation energy and stress exponent is commonly observed as the stress is raised [26–29]. The energy drop is commonly associated with a transition in the rate limiting step being from power-law creep of the carbide skeleton, to a grain boundary sliding mechanism. The transition usually occurs at ~200 MPa when tested at 1100–1200 °C [26–28]. However, there is insufficient literature data at 1000 °C for comparison to this study. Despite this, it is reasonable to expect the stress required for grain boundary sliding would decrease as the temperature is raised. Therefore, the onset of WC localised deformation and significant deformation bands seen here may be interpreted as indicative of grain boundary sliding.

3.3. Grain and phase boundaries

There are three boundary types: WC; Co_{fcc} and Co_{hcp}, resulting in six misorientation distributions for each binary combination of phases, WC/WC, WC/Co_{fcc}, WC/Co_{hcp}, Co_{fcc}/Co_{fcc}, Co_{fcc}/Co_{hcp}, and Co_{hcp}/Co_{hcp}. Note that only WC/WC, WC/Co_{fcc} and WC/Co_{hcp} are included here, as only these boundaries had sufficient boundary length fraction (>4 % for all samples) to be evaluated. Therefore, the Co_{fcc}/Co_{fcc}, Co_{fcc}/Co_{hcp}, and Co_{hcp}/Co_{hcp} boundaries, which did not meet this prevalence criterion, have been included in Supplementary Fig. 3.

The three relevant distribution types are shown in Fig. 7 for all samples. The prevalence of each boundary type, normalised by boundary length, is shown in the top-left of each sub-plot for the reference state only. The three boundary types involving WC dominate the overall fraction of boundaries; they contain between 82 and 97 % of the overall boundaries. Their high prevalence is due to the much smaller size of WC

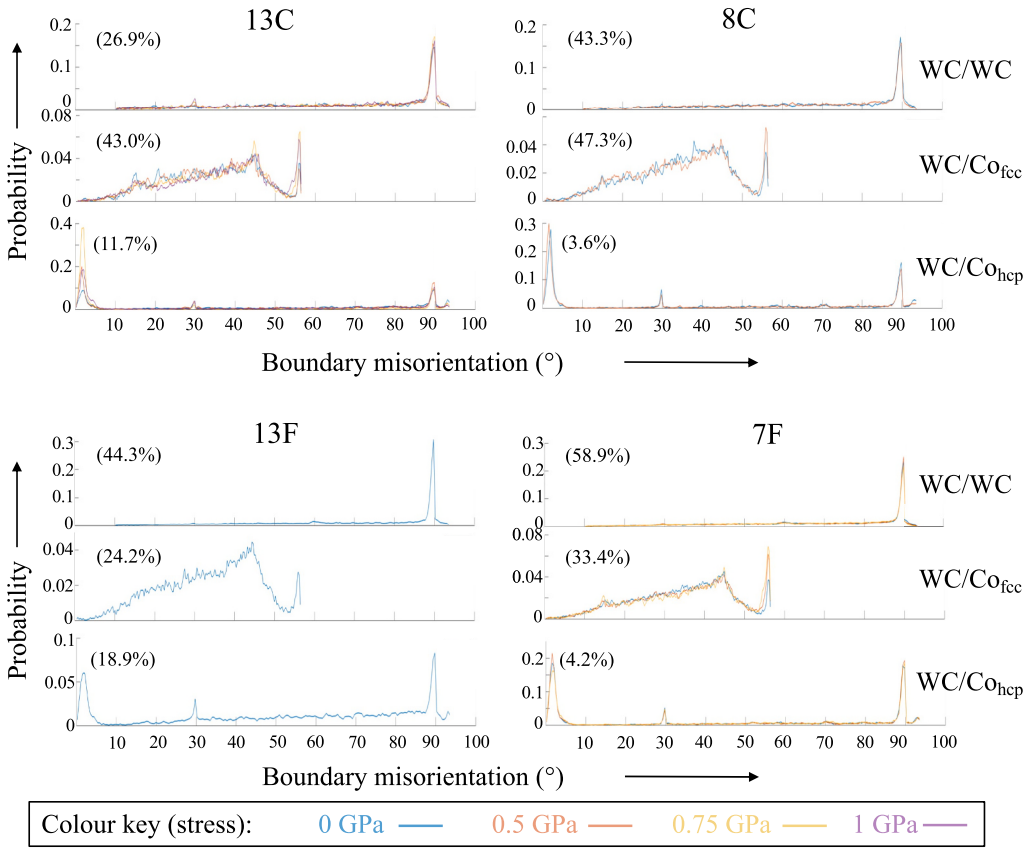

Fig. 7. Grain and phase boundary misorientation distributions for the WC/WC, WC/Co_{fcc} and WC/Co_{hcp} boundaries in each sample for different creep loads. The boundary prevalence in the reference state is indicated in brackets in the top-left of each plot. NB: for the WC/Co_{fcc} relationship, 0 degrees is taken to be the following orientation relationship: $(001)_{WC}$ // $(111)_{Co}$.

domains vs. Co ones (each map only between 2 and 10 distinct Co grains). The sum of all grain boundaries do not add up to exactly 100 %, due to a small presence of un-indexed pixels, partly due to pores or voids, which account for ~2 % of the fine materials (13F and 7F) and ~ 4 % of the coarse materials (8C and 13C). The sum of all boundaries did not change significantly for different levels of stress, thus only the reference state is reported.

Considering first the effects of stress on the WC/WC boundaries: The reference distributions are dominated by a large peak at 90° consistent with the Σ2 boundary, a twist boundary about the {10$\bar{1}$0} habit planes [30]. We also see smaller peaks at 30 and 60°, which are more noticeable in the finer-grained samples. These small peaks can be associated to mis-indexing, where two EBSD patterns of the related orientations are indexed in one grain as belonging to one or the other orientation. This is easily identified in orientation maps, such as those shown in Fig. 5(a), where within a single grain the orientation flips between the two orientations related by symmetry. These misorientation peaks have been associated to the Σ13 and Σ4 boundaries [30]; however, their presence is due to mis-indexing. There is no measurable effect of stress in the distributions. This suggests that WC's 90°-Σ2-grain boundary, is a particularly stable interface that remained unperturbed by deformation, as was also observed by Yuan et al. [9].

For the WC/Co_{fcc} boundaries, a uniquely broad probability distribution is seen in the range 0–60° misorientation. This is due to the mismatch of both cubic and hexagonal structures. The distribution between WC (hcp) and Co_{fcc} follows the characteristic density of random misorientation between cubic and hexagonal crystals (see Supplementary Fig. 2 for an example fit) [31]. Furthermore, there is a clear peak at ~56° misorientation, suggesting a slightly lower-energy configuration between WC and Co_{fcc} at this angle. The frequency of 56° misorientations of the WC/Cofcc boundary shows a clear and monotonic increase with increasing deformation in all samples, being close to 54.7 degrees, which is the angle for the $(100)_{WC}$ // $(111)_{Co}$ orientation relationship (within the measurement error). It is therefore possible that these 56° boundaries are preferentially formed when WC/WC boundaries are infiltrated with Co.

Finally, for the WC/Co_{hcp} boundaries, two peaks are seen at ~2 and 90°, with a small but measurable peak at 30°. It is interesting to note the prevalence of this boundary is 3–4 times greater in the higher Co content samples.

3.4. Creep voids

Fig. 8 shows SEM micrographs of all deformed samples. The compressive loading axis runs vertically in the visible cross-sections. Voids are seen in the 0.75 GPa and 1 GPa samples, but no voids were seen at 0.5 GPa in any of the samples. The onset of void formation thus correlates with the onset of significant inhomogeneous deformation in the WC phase, as shown in the KAM maps (Fig. 3), and the IPF maps (Fig. 5). The voids in the 13C sample are well dispersed, however those in the 7F sample appear to cluster together in groups (one of which is shown in the magnified inset), suggesting that significant strain localisation occurs in this grade. The voids themselves have an orientation dependence with respect to the loading axis, a point that is analysed quantitatively in Fig. 9.

The formation of intergranular creep voids during deformation of WC-Co has been reported extensively [19,29,32,33]. Generally, at interfaces and triple points, this movement is accounted for by the infiltration of the matrix, resulting in Co lamellae. However, according to Yousfi et al., unaccommodated grain boundary sliding and/or separation of adjacent hard particles is the cause of intergranular microvoids

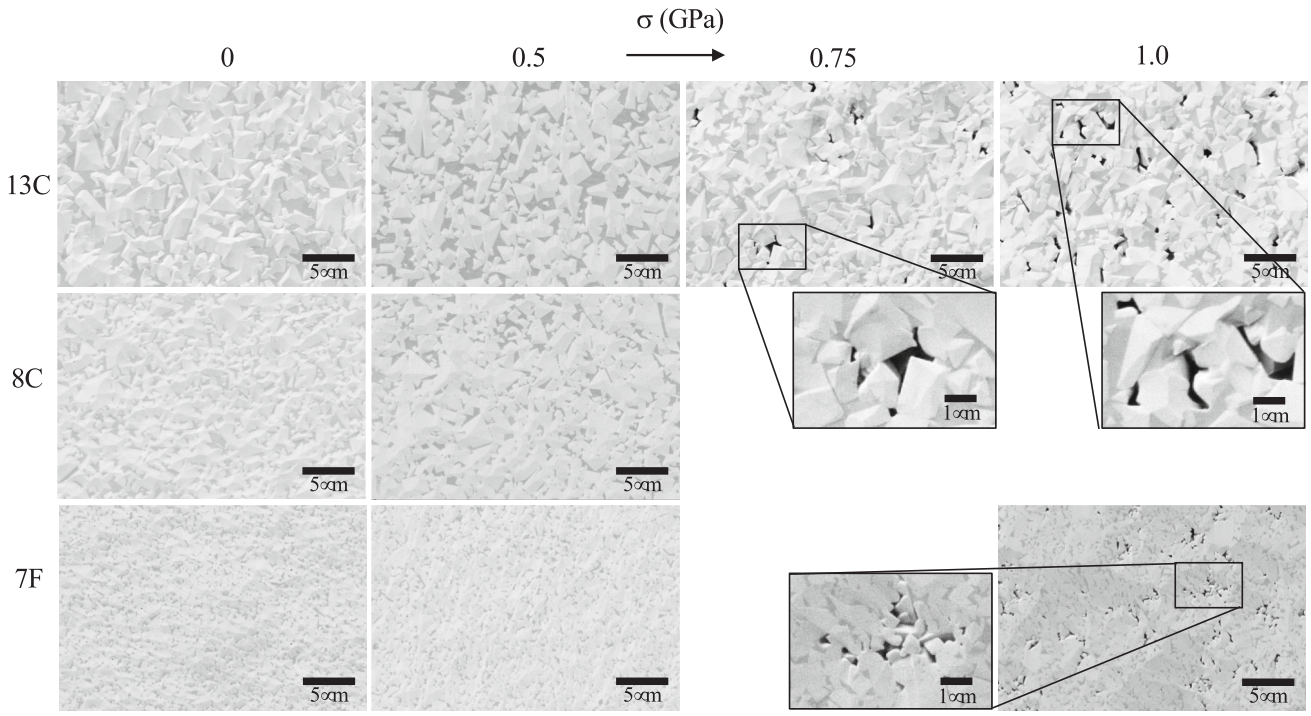

Fig. 8. Secondary electron SEM images of all deformed samples depicting the formation of microvoids in the cobalt matrix at 0.75 GPa and above. Images are oriented such that the compressive stress axis runs vertically.

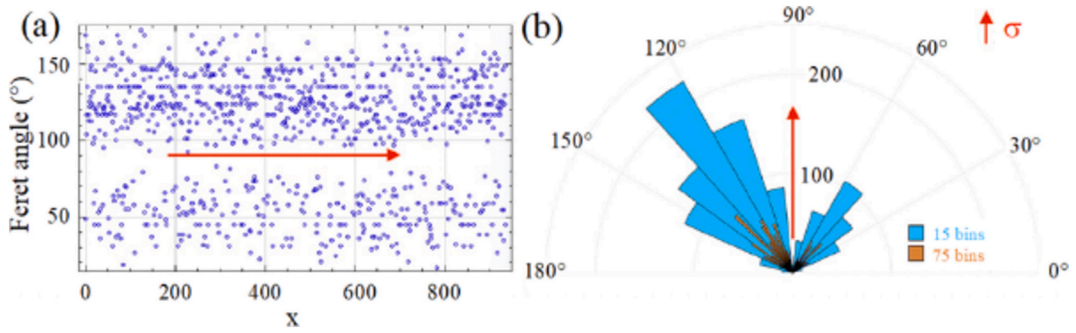

Fig. 9. The angle between the long axis of the microvoids and an axis perpendicular to the deformation axis (Feret angle) is plotted as a) a Cartesian frequency graph and b) a polar rose plot for the 13C-1GPa sample. Data in the rose plot is presented as 15 (blue) and 75 (orange) bins. (For interpretation of the references to colour in this figure legend, the reader is referred to the web version of this article.)

[18,34]. Alternatively, regions of high triaxial stress within the soft binder also preferentially nucleate cavities [19]. Table 3 shows the average area of each microvoid and their area fraction within the microstructure.

The orientation distribution of the micro-voids is shown in Fig. 9 for the 13C sample subjected to 1 GPa of stress. Most of the micro-voids formed during creep were elongated and demonstrated an orientation relationship with the deformation axis. This is because upon compressive stress there is an induced orthogonal tensile force, resulting in the highest resolved shear stresses occurring at inclinations of ±45° from the load direction.

To compare our results on void formation onset (Fig. 8 & Table 3) and changes in the mean KAM of the WC phase (Fig. 3), the two properties are both plotted as a function of strain in Fig. 10. Void formation (filled black symbols) occurs only when the strain exceeds about 10 %. Meanwhile, the increase in the mean KAM of the WC phase (red symbols) also only becomes significant when the strain exceeds a similar threshold, suggesting the two phenomena are indeed linked. It should be noted that the level of strain required to induce void formation is somewhat higher than in previous works. For example, Maier et al. [29] found that under compressive loading (350–1350 MPa) at 800 °C, a WC-12Co material (0.4 μm average grain size) formed voids at much lower strains of 0.2–3.3 %. The higher strains required in this study may be due to the significantly higher testing temperatures, which may enable the Co binder to accommodate more deformation before plasticity needs to be partitioned into the WC phase.

Table 3
Average size and area fraction of microvoids found in the samples. Uncertainty in area and area fraction are given by the standard deviation in values measured at 2 K, 5 K, and 10 K images. The presence of no voids is demarked "n.v.".

Material	Stress (GPa)	Average area (μm^2)	Area fraction (%)
7F	0.5	n.v.	
7F	1.0	0.1 ± 0.06	1.49 ± 0.40
8C	0.5	n.v.	
13C	0.5	n.v.	
13C	0.75	0.26 ± 0.11	0.8 ± 0.10
13C	1.0	0.26 ± 0.07	2.01 ± 0.09

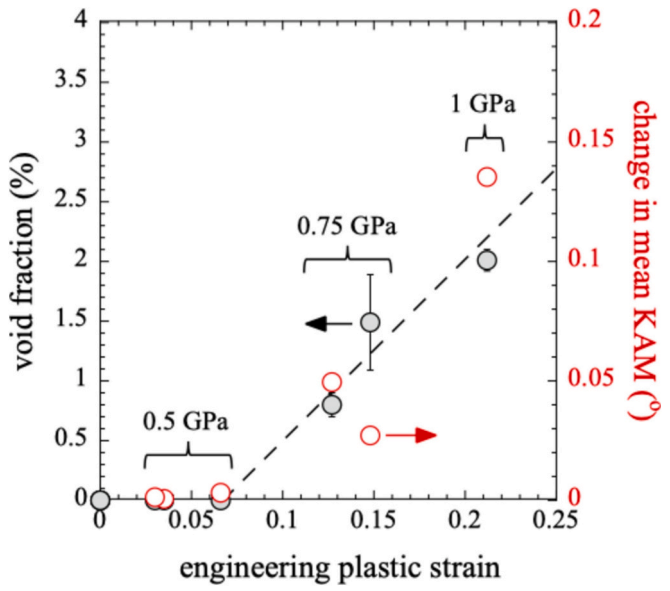

Fig. 10. The trend of microvoid % and the increase in the average KAM of the WC phase compared to the reference state (data from Supplementary Fig. 1). Both show minimal change up to ~10 % engineering plastic strain, beyond which there is strong increase.

4. Conclusions

Four grades of WC-Co were characterised by EBSD after creep deformation at 1000 °C in the stress range 0.5–1 GPa and plastic strains of 3–21 %. The localised strains within the microstructure, changes in grain boundary character, and formation of creep voids were characterised.

The KAM analysis suggests that at lower applied stresses (0.5 GPa), deformation within the grains was limited to the Co binder, while at higher stresses of 0.75 GPa and above significant localised deformation was observed in both phases. Such deformation was visible in localised bands radiating between neighbouring grains that are impinging on one another.

The IPF analysis confirmed this conclusion, demonstrated a spreading of orientations with Co grains even at 0.5 GPa. The spreading was exacerbated with increasing stress of 0.75 GPa and above in both phases.

Of the six types of grain boundary, two could be demonstrated to have distinct changes with creep: the 56° misorientation of the WC/Co_{FCC} boundary and the 60° misorientation of the Co_{FCC}/Co_{FCC} boundary. The latter is well studied and the result of a low energy coherent twin boundary, an efficient mechanism to accommodate large creep strains in a constrained microstructure. The increase in 56° WC/Co_{FCC} phase boundaries is likely due to the formation of a $(100)_{WC}$ // $(111)_{Co}$ orientation relationship. To the author's knowledge this was not previously reported, and may be related to the process of boundary infiltration. Further work is needed to confirm this point, which may involve understanding how the boundaries of this orientation relationship are dispersed within the microstructure, and how, if at all, they correlate with voids.

The orientation distribution of formed microvoids had a distinct orientation relationship with the deformation axis, likely due to the direction of resolved shear stresses within the material. Such void formation was a strong function of creep strain, which only became significant beyond a strain of 10 %. This coincided with the onset of significant increase in mean KAM within the WC grains, suggesting that microvoid formation and localised strain are strongly coupled and may coincide with a change in the dominant deformation mechanism.

CRediT authorship contribution statement

L. Weller: Writing – original draft, Visualization, Investigation. **R. M'saoubi:** Writing – review & editing, Investigation, Conceptualization. **F. Giuliani:** Writing – review & editing. **S. Humphry-Baker:** Writing – review & editing, Supervision, Conceptualization. **K. Marquardt:** Writing – review & editing, Supervision, Conceptualization.

Declaration of competing interest

The authors declare that they have no known competing financial interests or personal relationships that could have appeared to influence the work reported in this paper.

Data availability

Data will be made available on request.

Appendix A. Supplementary data

Supplementary data to this article can be found online at https://doi.org/10.1016/j.ijrmhm.2024.106950.

References

[1] A. Bose, A perspective on the earliest commercial pm metal-ceramic composite: cemented tungsten carbide, Int. J. Powder Metall. 47 (2011).
[2] G. Östberg, H.-O. Andrén, Microstructural changes during wear by plastic deformation of cemented carbide and cermet cutting inserts, Metall. Mater. Trans. A 37 (2006) 1495–1506.
[3] D. Mari, S. Bolognini, G. Feusier, T. Viatte, W. Benoit, Experimental strategy to study the mechanical behaviour of hardmetals for cutting tools, Int. J. Refract. Met. Hard Mater. 17 (1999) 209–225.
[4] S. Lay, J. Vicens, F. Osterstock, High temperature creep of WC-co alloys, J. Mater. Sci. 22 (1987) 1310–1322.
[5] K. Mingard, S. Moseley, S. Norgren, H. Zakaria, D. Jones, B. Roebuck, Microstructural observations of high temperature creep processes in hardmetals, Powder Metall. 64 (2021) 97–107, https://doi.org/10.1080/00325899.2021.1877866.
[6] M. Christensen, G. Wahnström, Co-phase penetration of WC (101\= 0)/WC (101\= 0) grain boundaries from first principles, Phys. Rev. B 67 (2003) 115415.
[7] J.-D. Kim, S.-J.L. Kang, J.-W. Lee, Formation of grain boundaries in liquid-phase-sintered WC–co alloys, J. Am. Ceram. Soc. 88 (2005) 500–503.
[8] M. Pellan, S. Lay, J.-M. Missiaen, S. Norgren, J. Angseryd, E. Coronel, T. Persson, EBSD study to analyse mechanisms of phase boundary and grain boundary development in WC-co cemented carbides, Powder Metall. 60 (2017) 208–215.
[9] X. Yuan, G.S. Rohrer, X. Song, H. Chien, J. Li, C. Wei, Effect of plastic deformation on the Σ2 grain boundary plane distribution in WC–Co cemented carbides, Int. J. Refract. Met. Hard Mater. 47 (2014) 38–43.
[10] G. Östberg, M.U. Farooq, M. Christensen, H.-O. Andrén, U. Klement, G. Wahnström, Effect of∑ 2 grain boundaries on plastic deformation of WC–Co cemented carbides, Mater. Sci. Eng. A 416 (2006) 119–125.
[11] V. Jayaram, R. Sinclalr, Detection of thin intergranular cobalt layers in WC-Co composites by lattice imaging, J. Am. Ceram. Soc. 66 (1983) C-137.
[12] R. Useldinger, U. Schleinkofer, Creep behaviour of cemented carbides—influence of binder content, binder composition and WC grain size, Int. J. Refract. Met. Hard Mater. (2017) 170–175.
[13] S. Lay, J.-M. Missiaen, 1.03–microstructure and morphology of hardmetals, Comprehens. Hard Mater. (2014) 91.
[14] B. Roebuck, E.A. Almond, A.M. Cottenden, The influence of composition, phase transformation and varying the relative FCC and HCP phase contents on the properties of dilute Co W C alloys, Mater. Sci. Eng. 66 (1984) 179–194.
[15] X. Han, On the Plastic Deformation Mechanisms of WC-Co Alloys at High Temperature, PhD Thesis, 2006.
[16] L.S. Sigl, H.F. Fischmeister, On the fracture toughness of cemented carbides, Acta Metall. 36 (1988) 887–897, https://doi.org/10.1016/0001-6160(88)90143-5.
[17] M.A. Yousfi, Microstructure Development of WC-co Based Cemented Carbides during Creep Testing, Chalmers University of Technology, 2016. https://research.chalmers.se/en/publication/235796 (accessed September 18, 2019).
[18] M.A. Yousfi, J. Weidow, A. Nordgren, L.K.L. Falk, H.-O. Andrén, Deformation mechanisms in a WC–co based cemented carbide during creep, Int. J. Refract. Met. Hard Mater. 49 (2015) 81–87, https://doi.org/10.1016/j.ijrmhm.2014.07.016.
[19] R. Spiegler, H.F. Fischmeister, Prediction of crack paths in WC-Co alloys, Acta Metall. Mater. 40 (1992) 1653–1661, https://doi.org/10.1016/0956-7151(92)90108-Q.
[20] F. Bachmann, R. Hielscher, H. Schaeben, Texture analysis with MTEX–free and open source software toolbox, in: Solid State Phenomena, Trans Tech Publ, 2010, pp. 63–68.

[21] R. Bergmann, R.H. Chan, R. Hielscher, J. Persch, G. Steidl, Restoration of manifold-valued images by half-quadratic minimization, IPI 10 (2016) 281–304, https://doi.org/10.3934/ipi.2016001.
[22] T.B. Britton, A.J. Wilkinson, Measurement of residual elastic strain and lattice rotations with high resolution electron backscatter diffraction, Ultramicroscopy 111 (2011) 1395–1404, https://doi.org/10.1016/j.ultramic.2011.05.007.
[23] G. Nolze, A. Winkelmann, About the reliability of EBSD measurements: data enhancement, IOP Conf. Ser.: Mater. Sci. Eng. 891 (2020) 012018, https://doi.org/10.1088/1757-899X/891/1/012018.
[24] A. Krawitz, E. Drake, Residual stresses in cemented carbides—an overview, Int. J. Refract. Met. Hard Mater. 49 (2015) 27–35.
[25] T. Teppernegg, T. Klünsner, C. Kremsner, C. Tritremmel, C. Czettl, S. Puchegger, S. Marsoner, R. Pippan, R. Ebner, High temperature mechanical properties of WC–Co hard metals, Int. J. Refract. Met. Hard Mater. 56 (2016) 139–144, https://doi.org/10.1016/j.ijrmhm.2016.01.002.
[26] S. Lay, F. Osterstock, High temperature creep of pure tungsten carbide and WC-Co alloys with low cobalt volumic ratios, in: Deformation of Ceramic Materials II, Springer, 1984, pp. 463–471.
[27] T. Sakuma, H. Hondo, Plastic flow in WC-13wt.% Co at high temperatures, Mater. Sci. Eng. A 156 (1992) 125–130.
[28] F. Ueda, H. Doi, F. Fujiwara, H. Masatomi, Y. Oosawa, Tensile creep of WC-10% Co and WC-10% TaC-10% Co alloys at elevated temperatures, Trans. Jpn. Inst. Metals 16 (1975) 591–600.
[29] K. Maier, T. Klünsner, M. Krobath, P. Pichler, S. Marsoner, W. Ecker, C. Czettl, J. Schäfer, R. Ebner, Creep behaviour of WC-12 wt% Co hardmetals with different WC grain sizes tested in uniaxial tensile and compression step-loading tests at 700 °C and 800 °C, Int. J. Refract. Met. Hard Mater. 100 (2021) 105633, https://doi.org/10.1016/j.ijrmhm.2021.105633.
[30] S. Hagege, G. Nouet, P. Delavignette, Grain boundary analysis in TEM. IV. Coincidence and the associated defect structure in tungsten carbide, Phys. Status Solidi A 62 (1980) 97–107.
[31] V.I. Skrytnyy, V.N. Yaltsev, Relative misorientations of crystals, in: IOP Conference Series: Materials Science and Engineering, IOP Publishing, 2016, p. 012059.
[32] H.G. Schmid, D. Mari, W. Benoit, C. Bonjour, The mechanical behaviour of cemented carbides at high temperatures, Mater. Sci. Eng. A 105 (1988) 343–351.
[33] H. Zhang, J. Xiong, Z. Guo, T. Yang, J. Liu, T. Hua, Microstructure, mechanical properties, and cutting performances of WC-Co cemented carbides with Ru additions, Ceram. Int. 47 (2021) 26050–26062.
[34] D. Mari, Déformation à Haute Temperature des Composites WC-Co, EPFL, 1991.